Sacrificial Interlayer for Promoting Charge Transport in Hematite Photoanode

Kai Zhang,[†,§] Tianjiao Dong,[†,‡,§] Guancai Xie,[†,‡,§] Liming Guan,[†,§] Beidou Guo,[†,§] Qin Xiang,[†,‡] Yawen Dai,[†,‡] Liangqiu Tian,[†,‡] Aisha Batool,[†,‡] Saad Ullah Jan,[†,‡] Rajender Boddula,[†,‡] Akbar Ali Thebo,[†,‡] and Jian Ru Gong*,[†]

†Chinese Academy of Sciences (CAS) Center for Excellence in Nanoscience, CAS Key Laboratory of Nanosystem and Hierarchy Fabrication, National Center for Nanoscience and Technology, Beijing 100190, P. R. China

‡University of Chinese Academy of Sciences, Beijing 100049, P. R. China

Ⓢ Supporting Information

ABSTRACT: The semiconductor/electrolyte interface plays a crucial role in photoelectrochemical (PEC) water-splitting devices as it determines both thermodynamic and kinetic properties of the photoelectrode. Interfacial engineering is central for the device performance improvement. Taking the cheap and stable hematite (α-Fe$_2$O$_3$) wormlike nanostructure photoanode as a model system, we design a facile sacrificial interlayer approach to suppress the crystal overgrowth and realize Ti doping into the crystal lattice of α-Fe$_2$O$_3$ in one annealing step as well as to avoid the consequent anodic shift of the photocurrent onset potential, ultimately achieving five times increase in its water oxidation photocurrent compared to

the bare hematite by promoting the transport of charge carriers, including both separation of photogenerated charge carriers within the bulk semiconductor and transfer of holes across the semiconductor–electrolyte interface. Our research indicates that understanding the semiconductor/electrolyte interfacial engineering mechanism is pivotal for reconciling various strategies in a beneficial way, and this simple and cost-effective method can be generalized into other systems aiming for efficient and scalable solar energy conversion.

KEYWORDS: water splitting, photoelectrochemistry, hematite, confined growth, doping, charge transport
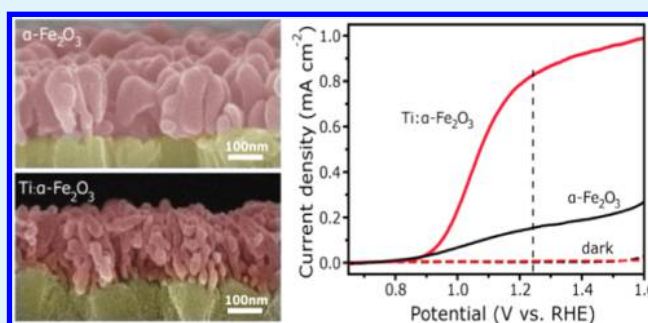
1. INTRODUCTION

Photoelectrochemical (PEC) water splitting represents one of the most promising solutions to the deteriorating global energy crisis and environmental problem.[1,2] Over 40 years, massive semiconductor materials have been reported to be active for PEC water splitting.[3−5] However, this technology is still far from commercialization primarily because of the unsatisfactory solar energy conversion efficiency as well as the cost and stability issues.[3−6] The performance of a PEC device, in theory, is determined collectively by its capabilities for incident photon absorption, charge separation within the bulk semiconductor, as well as interfacial charge transfer across the semiconductor–electrolyte interface.[7,8] Most of the reported PEC electrode materials possess excellent abilities in absorbing photons with energy larger than their band gaps.[4,5,9] Hence, the poor PEC performance of the photoelectrode materials, especially those anode materials for the kinetically slow water oxidation process,[10,11] should be largely attributed to the inefficient utilization of photogenerated charge carriers, which includes both the inferior separation of photogenerated charges inside the bulk semiconductor and the sluggish charge transfer across the semiconductor–electrolyte interface.[5]

The combination of multiple strategies has been adopted to strengthen the charge transport in semiconductor photoelectrodes.[12−14] Taking hematite (α-Fe$_2$O$_3$), a prospective low-cost photoanode material naturally endowed with a suitable valence band position for water oxidation, a favorable band gap (around 2.1 eV) for effective photon harvesting, and excellent chemical stability in a wide range of pH values,[15−18] as an example, its theoretical PEC water-splitting current density reaches up to 12.6 mA cm^{-2} under illumination of air mass 1.5 global (AM 1.5G) sunlight, potentially enabling a maximum solar energy conversion efficiency of 15.5% in an ideal tandem cell configuration.[16,18] But, owing to the problem of severe charge recombination, which results from its extremely short (ca. 10 nm) hole collection depth (hole diffusion length + space-charge layer width) and poor electron conductivity via small polaron hopping conduction with a low electron mobility ($<10^{-2}$ cm^2 V^{-1} s^{-1}), the reported photocurrent densities of α-Fe$_2$O$_3$ photoanodes are far below the theoretical value.[15,18−20]

Scheme 1. Schematic Synthetic Procedures for α-Fe$_2$O$_3$, TiO$_2$@Ti:α-Fe$_2$O$_3$, and Ti:α-Fe$_2$O$_3$ Photoanodes
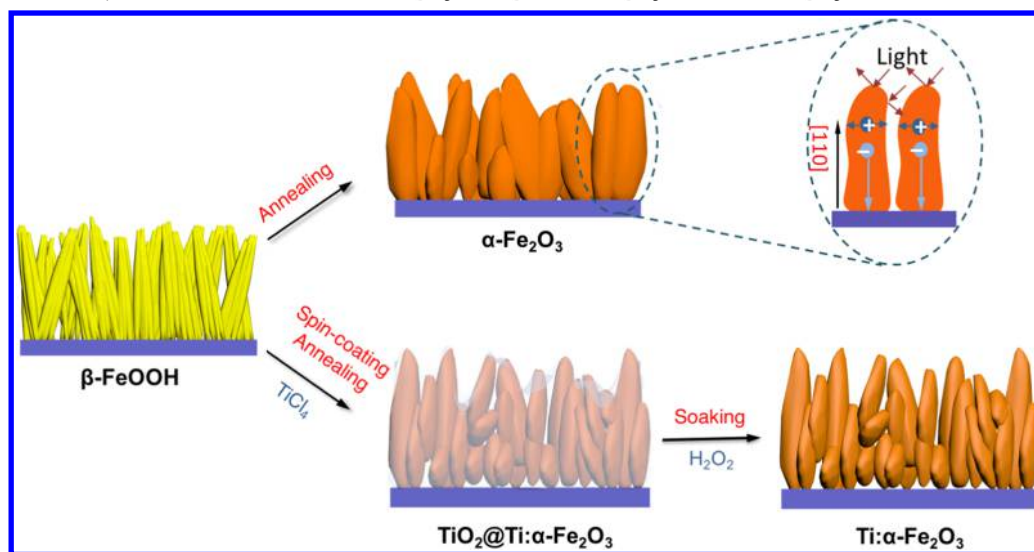
Geometry nanostructuring for shortening the collection distance of photogenerated holes and foreign elements doping for increasing the electron conductivity are common methods for improving the activity of α-Fe$_2$O$_3$ photoanodes.[21−24] For example, Wang et al. reported a Ti-doped α-Fe$_2$O$_3$ film photoanode by a facile deposition-annealing procedure, which gave a negative onset potential shift of 0.1−0.2 V and a photocurrent of 1.83 mA cm^{-2} at 1.02 V vs reversible hydrogen electrode (RHE).[24] A similar postgrowth doping was also developed to dope hematite nanowire photoanodes after growth and greatly enhanced their photoactivity for PEC water splitting.[23] Recently, Zheng and co-workers have also raised a flame doping method to enable a high concentration of Ti doping into hematite photoanode.[25] Nonetheless, high-temperature annealing is frequently required to promote the crystallinity of α-Fe$_2$O$_3$ nanocrystals and/or to facilitate the incorporation of dopants into their crystal lattices, and it will simultaneously cause the increase of the nanocrystal feature size or even damage the original nanostructure formed at low temperature.[19,26−28] Some progress has been made to tackle this long-standing problem.[25,26,29−33] For instance, Sivula et al. developed a solution-based SiO$_2$ confinement layer strategy to realize the independent control of the nanocrystal feature size and the dopant incorporation in the photoanode.[30] However, a considerable anodic shift of the photocurrent onset potential appeared, and the scale-up application of this method is also restricted due to the complicated two-step annealing procedure included.[15] Understanding the inherent interacting mechanisms and developing a facile and cost-effective technique to reconcile crystal size control with dopant incorporation together without consequent adverse effects are of crucial importance for high-efficient water-splitting PEC devices.

Herein, taking the α-Fe$_2$O$_3$ wormlike nanostructure photoanode as a model system, the common problem of crystal coarsening after annealing treatment for doping was overcome by realizing both suppression of crystal overgrowth and Ti doping in one step via a dopant-containing interlayer coating. After the thorough thermodynamic and kinetic analysis, the consequent anodic shift of the photocurrent onset potential was avoided by removing the interlayer through subsequent H$_2$O$_2$ soaking, ultimately achieving five times performance increase compared with the bare hematite by promoting transport of

charge carriers, including both separation of photogenerated charge carriers within the bulk semiconductor and transfer of holes across the semiconductor−electrolyte interface.

2. EXPERIMENTAL SECTION

2.1. Preparation of Photoanodes. The synthetic process of the Ti-doped α-Fe$_2$O$_3$ wormlike nanostructure photoanode (labeled as Ti:α-Fe$_2$O$_3$) is depicted in Scheme 1. First, the β-FeOOH thin film with nanorod morphology was grown on a fluorine-doped tin oxide (FTO)-coated glass substrate by a modified hydrothermal method.[34] Typically, 20 mL of aqueous solution containing 5 mmol FeCl$_3$ and 15 mmol NH$_2$CONH$_2$ was transferred into a Teflon-lined stainless steel autoclave, and an FTO-coated glass substrate was placed inside the autoclave with its conducting surface vertical to the bottom of the Teflon lining. Then, the autoclave was sealed and heated at 70 °C for 6 h, resulting in the formation of a yellowish β-FeOOH thin film on the FTO glass. Afterward, the β-FeOOH thin film was rinsed thoroughly with deionized water, blow-dried with nitrogen gas, spin-coated with 10 μL of TiCl$_4$ ethanol solution, and annealed at 600 °C for 30 min with a ramp-up rate of 5 °C min^{-1}, forming an orangish semitransparent photoanode. Here, we labeled it as x-TiO$_2$@Ti:α-Fe$_2$O$_3$ photoanode with x (=0.25, 0.5, 1.0, 1.5%) representing the volume fraction of TiCl$_4$ in the ethanol solution (TiO$_2$ formation and Ti doping will be evidenced in the Results and Discussion section). Finally, the Ti:α-Fe$_2$O$_3$ photoanode was obtained by removing the TiO$_2$ on the surface of the 0.5%-TiO$_2$@Ti:α-Fe$_2$O$_3$ photoanode via soaking it in a peroxide (H$_2$O$_2$) solution for 24 h. For comparison, a pristine α-Fe$_2$O$_3$ wormlike nanostructure photoanode was prepared via directly annealing the β-FeOOH thin film at 600 °C for 30 min in a muffle furnace.

2.2. Material Characterization. X-ray diffraction (XRD) patterns were recorded using an X'pert powder diffractometer with an operating voltage of 40 kV and an operating current of 40 mA to characterize the crystal structures of the prepared thin-film photoanodes, and the grazing incidence XRD mode was adopted for increasing the signal-to-noise ratio. The micromorphology of the photoanodes was examined by a Hitachi S-4800 field emission scanning electron microscope at an accelerating voltage of 10 kV. Transmission electron microscopy (TEM), high-angle annular dark-field scanning transmission electron microscopy (HAADF), and energy-dispersive spectroscopy (EDS) mapping experiment were carried out on an FEI Tecnai F20 field emission transmission electron microscope operated at 200 kV. The ultraviolet−visible (UV−vis) transmittance and reflectance spectra were obtained using a UV−vis spectrophotometer (UV-2600) equipped with an external diffuse reflectance accessory (DRA-2500), and the absorbance (A) was
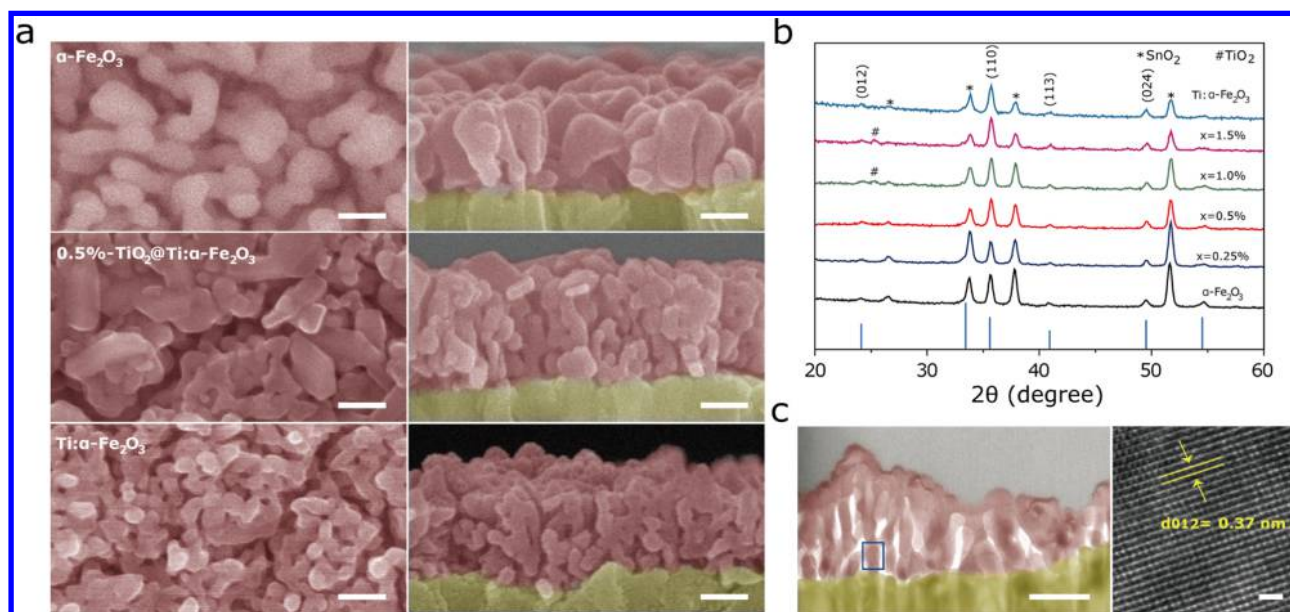
Figure 1. (a) Typical top-view (left column) and cross-sectional (right column) SEM images of α-Fe$_2$O$_3$, 0.5%-TiO$_2$@Ti:α-Fe$_2$O$_3$, and Ti:α-Fe$_2$O$_3$ photoanodes. The α-Fe$_2$O$_3$ and FTO layers are differentiated by grayish pink and yellow-green masks, respectively. The scale bar is 100 nm. (b) XRD patterns of α-Fe$_2$O$_3$, x-TiO$_2$@Ti:α-Fe$_2$O$_3$ (x = 0.25, 0.5, 1.0, and 1.5%), and Ti:α-Fe$_2$O$_3$ photoanodes. The blue lines highlight the diffraction peaks of the hematite crystal structure (PDF Card No. 87-1166). (c) Cross-sectional TEM overview (scale bar, 100 nm) of the 0.5%-TiO$_2$@Ti:α-Fe$_2$O$_3$ photoanode and HRTEM image (scale bar, 1 nm) of the selected area in TEM image.

calculated by the formula $A = 1 - T - R$, where T is the total transmittance and R is the total reflectance. The physical surface area of the hematite films was determined by adsorption of the azo dye Orange II, which had been shown to form a monolayer on the nanocrystalline α-Fe$_2$O$_3$ at a concentration of 1.5 mM in the water solution with pH 3.5 after HCl addition, occupying an area of 0.40 nm^2 per dye molecule.[35,36] The electrodes with the geometrical area of 0.636 cm^2 were exposed to the Orange II aqueous solution for 15 min and then the adsorbed dye was desorbed in 5 mL of 1 M NaOH solution and subjected to a UV−vis spectrophotometer (UV-2600) to measure its amount by recording the absorbance at 450 nm. X-ray photoelectron spectroscopy (XPS) and valence band spectra measurements were conducted in an ultrahigh vacuum system equipped with a monochromatic Al Kα (1486.6 eV) source (Thermo Scientific Escalab 250Xi).

2.3. Photoelectrochemical Measurements. All of the photoelectrochemical measurements were carried out in an electrochemical workstation (Zahner Zennium, Germany) in a typical three-electrode configuration with the prepared photoanode as the working electrode, a Pt foil as the counter electrode, a saturated Ag/AgCl electrode as the reference electrode, and 1 M NaOH (pH = 13.6) aqueous solution as the electrolyte. The samples with the geometrical area of 0.636 cm^2 were illuminated with simulated AM 1.5G sunlight generated from a 500W xenon lamp equipped with an AM 1.5G filter (CEL-S500, Aulight, Beijing, China), and the light density was calibrated to be 100 mW cm^{-2} (1 Sun). The photocurrent density−applied potential (J−V) plots of the photoanodes were scanned at 37 mV s^{-1} between −400 and 700 mV vs the saturated Ag/AgCl electrode. For the light chopped J−V plots, the chopping frequency was ~2 Hz. Mott−Schottky measurements were performed on all of the photoanodes in the dark with the same three-electrode cell in 1 M NaOH solution. The donor concentration (N_d) was calculated by the Mott−Schottky equation

$$\frac{1}{C^2} = \frac{2}{AN_d e \varepsilon \varepsilon_0}\left(V - V_{FB} - \frac{kT}{e}\right)$$

(1)

wherein C is the space-charge capacitance, A is the physical surface area of the electrode, e is the elementary charge, ε is the dielectric constant of hematite (80), ε_0 is the vacuum permittivity, V is the applied potential, V_{FB} is the flat-band potential, k is the Boltzmann

constant, and T is the absolute temperature. Electrochemical impedance spectra (EIS) at a direct current potential of 0.23 V vs Ag/AgCl were recorded under simulated AM 1.5G sunlight illumination condition at frequencies from 100 000 to 0.1 Hz with a sinusoidal potential perturbation of 10 mV. EIS data were fitted according to a classical equivalent circuit model using ZSimpWin software. The photovoltage measurements were conducted in the same three-electrode configuration with O$_2$ bubbling into the electrolyte under illumination of a 150 W xenon lamp (Crown Tech., CT-XE-150) with a light intensity of ~450 mW cm^{-2}. Each dark−light open-circuit potential reading was obtained after a 30 min stabilization process with constant stirring.[37,38] A Si photodiode with known incident photon-to-photocurrent efficiencies (IPCEs) was used to calculate the IPCEs of the hematite photoanodes, and a source meter (Keithley 2400) was used to measure the photocurrents of the Si photodiode and the photoanodes (here, the photocurrent of the photoanodes is obtained by subtracting the dark currents from their currents under illumination). The IPCE values of the photoanodes were calculated using the following equation

$$IPCE_{photoanode} = \frac{photocurrent_{photoanode} \times IPCE_{Si}}{photocurrent_{Si}}$$

(2)

All of the measured potentials against the saturated Ag/AgCl electrode were converted to the reversible hydrogen electrode (RHE) scale according to the Nernst equation

$$E_{RHE} = E_{Ag/AgCl} + 0.059 \times pH + E^0_{Ag/AgCl}$$

(3)

wherein E_{RHE} is the converted potential vs RHE, $E_{Ag/AgCl}$ is the measured potential against the saturated Ag/AgCl electrode, and $E^0_{Ag/AgCl}$ is the standard potential of the saturated Ag/AgCl electrode (0.197 V at 25 °C). IPCE values from 350 to 650 nm were measured at a potential of 0.23 V vs Ag/AgCl (1.23 vs RHE) using the above 150 W xenon lamp equipped with a monochromator (M24-D).

2.4. Calculation of Charge Separation and Injection Efficiencies. The charge separation efficiency (η_{sep}) represents the yield of the photogenerated holes that reach the semiconductor−electrolyte interface without bulk recombination. The charge injection efficiency (η_{inj}) describes the yield of the photogenerated holes that are successfully injected into the electrolyte to trigger water oxidization
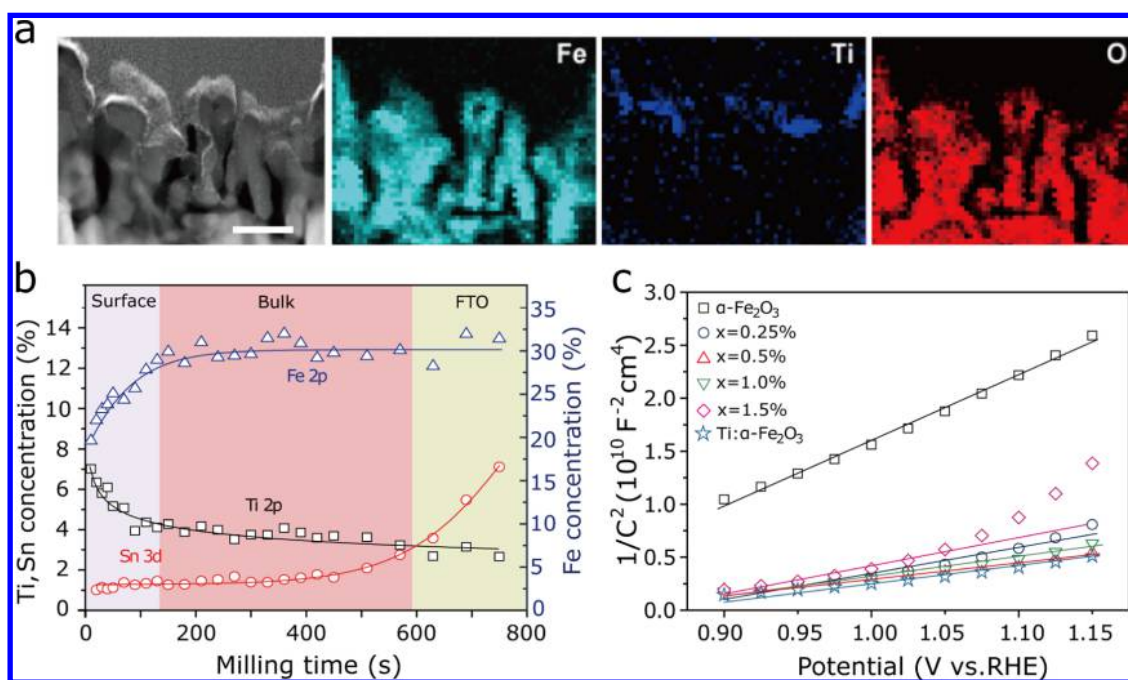
Figure 2. (a) HAADF-STEM image and EDS mapping results of Fe, Ti, and O elements in the 0.5%-TiO$_2$@Ti:α-Fe$_2$O$_3$ photoanode. The scale bar is 100 nm. (b) XPS depth profiling of the Fe, Ti, and Sn elements in the 0.5%-TiO$_2$@Ti:α-Fe$_2$O$_3$ photoanode as a function of the Ar$^+$ ion milling time. The mauve pale, grayish pink, and yellow-green shades represent the surface TiO$_2$, bulk Ti-doped α-Fe$_2$O$_3$, and FTO substrates, respectively. (c) The Mott−Schottky curves of the α-Fe$_2$O$_3$, x-TiO$_2$@Ti:α-Fe$_2$O$_3$ (x = 0.25, 0.5, 1.0, and 1.5%), and Ti:α-Fe$_2$O$_3$ photoanodes are plotted together for a clear comparison of the change in their slopes.

without recombining with the electrons at surface trap states. By assuming the charge injection efficiency to be 100% in the presence of the hole scavenger (H$_2$O$_2$) in the electrolyte, these two efficiencies were calculated using the following equations[7]

$$\eta_{sep} = J_{H_2O_2}/J_{absorbed} \tag{4}$$

$$\eta_{inj} = J_{H_2O}/J_{H_2O_2} \tag{5}$$

where $J_{H_2O_2}$ is the photocurrent density gained with the addition of the hole scavenger (0.5 M H$_2$O$_2$) to the 1 M NaOH solution, J_{H_2O} is the water oxidation photocurrent density in 1 M NaOH solution, and $J_{absorbed}$ is the photon absorption rate expressed as a current density, which can be calculated by using the following equation[39]

$$J_{absorbed} = \frac{e}{hc} \times \int_{\lambda_a}^{\lambda_b} P_{(\lambda)} A_{(\lambda)} \lambda \, d\lambda \tag{6}$$

where λ_a is the shortest wavelength of the light emitted by the light source; λ_b is the wavelength of the absorption edge of the photoelectrode; and P, λ, h, c, e, and A are the power of incident photons, the wavelength of incident monochromatic light, the Planck constant, the speed of light, the elementary charge, and the absorbance of the photoelectrode, respectively.

3. RESULTS AND DISCUSSION

The α-Fe$_2$O$_3$ photoanode with wormlike nanostructures was selected as a model system in our experiment because its highly conductive [110] basal planes perpendicular to the substrate can provide a direct conducting pathway for electrons to efficiently migrate to the underlying conductive substrate (Scheme 1).[34,40] Ti was chosen as the model dopant considering its strong capability of promoting the PEC water oxidation activity of the α-Fe$_2$O$_3$ photoanode without causing large distortion in the crystal lattice.[41]

Bundles of nanorods with a diameter of about 40 nm are uniformly grown on the FTO substrate after the hydrothermal

treatment (SEM images in the first row of Figure S1) and are confirmed to be β-FeOOH according to the akaganeite crystal structure (black pattern in Figure S2). After thermal annealing at 600 °C, these β-FeOOH nanorod bundles are transformed into perpendicularly aligned podgy nanostructures with diameters of about 50−90 nm on the FTO substrate (SEM images in the first row of Figure 1a and Figure S3a), and only the diffraction peaks of the hematite crystal structure (PDF Card No. 87-1166) can be found in the corresponding XRD pattern of this sample except those belonging to the FTO substrate, indicating the complete transformation of β-FeOOH into α-Fe$_2$O$_3$ (black pattern in Figure 1b). Meanwhile, the intensity of the hematite (110) diffraction peak is distinctly higher than that of the other peaks, verifying the expected [110] preferential orientations of the hematite nanostructure.[37] When the ethanol solutions with different volume fractions of TiCl$_4$ (x = 0.25, 0.5, 1.0, and 1.5%) are spin-coated onto the β-FeOOH film, a thin and uniform coating layer, through which one can see the well-preserved nanorod bundles of β-FeOOH, is evident from the typical SEM images in the second row of Figure S1, and the akaganeite crystal structure of β-FeOOH is also retained according to the red XRD pattern in Figure S2. After thermal annealing of these TiCl$_4$-coated β-FeOOH thin films, all of the XRD patterns of the x-TiO$_2$@Ti:α-Fe$_2$O$_3$ photoanodes remain similar to those of the α-Fe$_2$O$_3$ photo-anode (Figure 1b), suggesting that TiCl$_4$ has little effect on both the crystal structure and preferential orientation of these hematite photoanodes. However, the morphology of the x-TiO$_2$@Ti:α-Fe$_2$O$_3$ photoanodes is quite different from that of the α-Fe$_2$O$_3$ photoanode. For the typical 0.5%-TiO$_2$@Ti:α-Fe$_2$O$_3$ photoanode, the feature size is about 30−50 nm, much smaller than that of the α-Fe$_2$O$_3$ photoanode (second row in Figure 1a, and Figure S3b). That is, the coarsening of the α-Fe$_2$O$_3$ nanostructure during thermal annealing treatment,
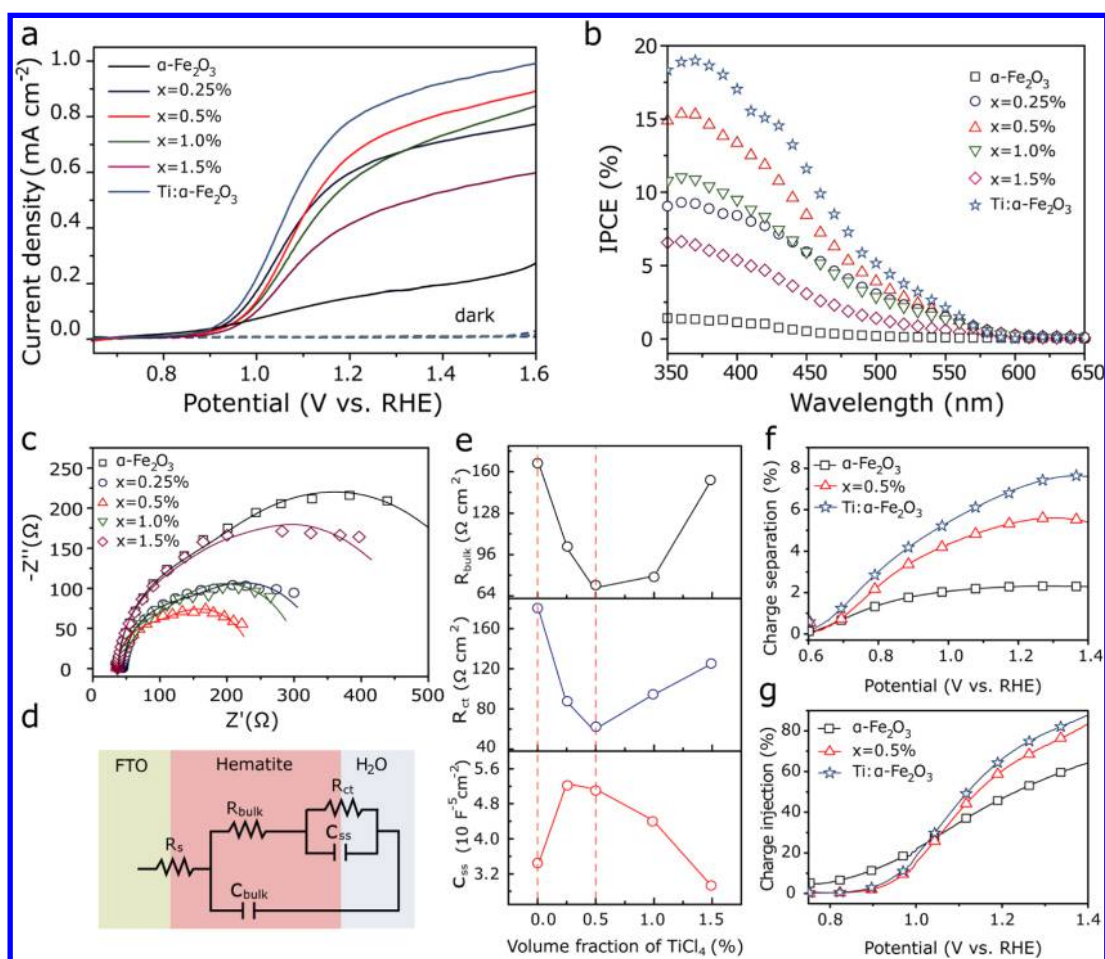
Figure 3. (a) $J-V$ plots in dark (dotted curves) and under illumination of simulated AM 1.5G sunlight (solid curves) and (b) IPCE curves of α-Fe_2O_3, x-$TiO_2@Ti:\alpha$-Fe_2O_3 (x = 0.25, 0.5, 1.0, and 1.5%), and $Ti:\alpha$-Fe_2O_3 photoanodes at a bias of 1.23 V vs RHE. (c) Nyquist plots of α-Fe_2O_3 and x-$TiO_2@Ti:\alpha$-Fe_2O_3 (x = 0.25, 0.5, 1.0, and 1.5%) photoanodes at a bias of 1.23 V vs RHE under the illumination of simulated AM 1.5G sunlight. (d) Classical physical equivalent circuit model of the hematite–electrolyte interface employed for EIS fitting. (e) Changes in the values of R_{bulk}, R_{ct}, and C_{ss} as a function of the volume fraction of $TiCl_4$ in the spin-coated ethanol solution. (f) Charge separation and (g) charge injection efficiencies of α-Fe_2O_3, 0.5%-$TiO_2@Ti:\alpha$-Fe_2O_3, and $Ti:\alpha$-Fe_2O_3 photoanodes.

which is apparent in the α-Fe_2O_3 photoanode, has been effectively suppressed after spin-coating the $TiCl_4$ ethanol solution. TEM analysis on a cross-sectional specimen prepared using focused ion beam (FIB) "lift-out" technique was also performed to gain a deeper insight into the nanostructure of this photoanode.[42] The overview image in Figure 1c clearly shows the alignment of upward-growing wormlike hematite nanostructure on the FTO substrate, whose diameters are around 30–50 nm, being consistent with the sizes in the SEM images. Moreover, the lattice fringes with a d-spacing of 0.37 nm, which can be indexed to the (012) planes of the hematite crystal structure, are distinct in the high-resolution TEM (HRTEM) image of the marked area in Figure 1c, demonstrating the high crystallinity of the hematite nanostructures. Besides, according to the existence of a strong Ti 2p peak with binding energy equal to that of TiO_2 in the XPS images of all of the x-$TiO_2@Ti:\alpha$-Fe_2O_3 photoanodes[43] (Figure S3 and Table S1) and the appearance of anatase TiO_2 (101) diffraction peak at 25.3° when the volume fraction of $TiCl_4$ in the ethanol solution is higher than 0.5% (Figure 1b), we suppose that there should be a TiO_2 encapsulation layer formed on the surface of the x-$TiO_2@Ti:\alpha$-Fe_2O_3 photoanodes. Accordingly, the change in the feature size of the hematite nanostructures in the x-

$TiO_2@Ti:\alpha$-Fe_2O_3 photoanodes could be attributed to the presence of the TiO_2 encapsulation layer, which acts as a powerful confinement layer during the thermal annealing process, effectively restraining the coarsening of the hematite nanostructure.[30]

STEM-EDS mapping analysis and XPS depth profiling were conducted to explore the elemental distribution in the 0.5%-$TiO_2@Ti:\alpha$-Fe_2O_3 photoanode. Figure 2a displays the HAADF-STEM image of the cross-sectional specimen, together with the EDS mapping results for the Fe, Ti, and O elements. Both the Fe and O elements distribute uniformly in the thin-film photoanode, whereas Ti atoms mainly accumulate on the top of hematite nanostructures accompanied with the diffusion of a few atoms into the bulk of the 0.5%-$TiO_2@Ti:\alpha$-Fe_2O_3 photoanode. In Figure 2b, the concentration of the Ti element decreases from 7 to 4% rapidly with the increase of Ar^+ ion milling time from 0 to 100 s, then stabilizes at a concentration of around 3% during the subsequent ion milling process, and the concentration of the Sn element greatly increases when the ion milling time exceeds 500 s, suggesting that the ion-milled surface is getting closer to the α-Fe_2O_3/FTO interface (here, the small amount of Sn detected in the initial 400 s should be originated from the FTO substrate exposed to X-ray during

XPS measurement because no Sn signal, which is not shown, was collected in EDS mapping analysis[33]). The high surface atomic concentration of Ti element with a Ti-to-Fe atomic ratio (37%) higher than that of the solubility of TiO_2 in α-Fe_2O_3 at 1000 °C (5%) is in accordance with the accumulation of Ti atoms on the top of hematite nanostructures in the EDS mapping result, further proving the formation of the TiO_2 encapsulation layer on the surface of the 0.5%-TiO_2@Ti:α-Fe_2O_3 photoanode.[44] Meanwhile, Ti signal detected at the position close to the α-Fe_2O_3/FTO interface also implies the diffusion of Ti atoms into the 0.5%-TiO_2@Ti:α-Fe_2O_3 photoanode, again being consistent with the above EDS mapping result. We infer that the Ti atoms are doped into the hematite nanostructures as the concurrent thermal diffusion of Ti atoms and dehydration of β-FeOOH taking place during the thermal annealing treatment make the incorporation of Ti atoms into the crystal lattice of α-Fe_2O_3 much more effective and easier.[25]

Foreign element doping can increase the donor concentration in the α-Fe_2O_3 host material, which probably promotes the conductivity of the photoanode.[45] Therefore, we measured the Mott−Schottky plots of all of the photoanodes to investigate the changes in their donor concentrations as well as to verify the doping of Ti atoms into the hematite. The Mott−Schottky relationship, in theory, is derived assuming a perfectly flat electrode surface; therefore, care must be taken when analyzing and interpreting the data from rough surfaces. Nonetheless, for a nanostructured electrode, it has been reported that the linearity of the Mott−Schottky plot can be held if the diameters of the nanostructured building blocks of the electrode are much larger than the thickness of the space-charge layer and the electrode area in the Mott−Schottky equation is taken to be the physical surface area rather than the geometrical area of the electrode.[46] We note that the feature sizes of the nanostructures in our prepared photoanodes (Figure 1a) are all sufficiently larger than the thickness of the space-charge layer ($\approx$7 nm).[25] So the carrier concentrations and flat-band potentials of these photoanodes can be explicitly obtained via extracting the slopes and intercepts of the linear parts in their Mott−Schottky plots.[23,47] As shown in Figures 2c and S5, the n-type conductive nature of all of the photoanodes is evident from the positive slopes of their Mott−Schottky plots and the slopes of the Mott−Schottky plots of the x-TiO_2@Ti:α-Fe_2O_3 photoanodes are all smaller than those of the α-Fe_2O_3 photoanode, demonstrating the increase in the carrier concentration because of Ti doping. Here, it should be noted that the effects of the underlying FTO substrate on the carrier concentrations should be similar for all of the prepared photoanodes because of the identical thermal annealing conditions and that the doping effect of Sn atoms can also be excluded according to the absence of Sn signals in EDS mapping results. We calculated the carrier concentrations of the α-Fe_2O_3 (0.68×10^{16} cm^{-3}) and 0.5%-TiO_2@Ti:α-Fe_2O_3 (1.86×10^{16} cm^{-3}) photoanodes using the physical surface areas of the electrodes determined by Orange II dye adsorption measurements (Figure S6).[35,36] The doping of Ti into hematite nanostructures has led to a carrier concentration 2 times the magnitude of that of the α-Fe_2O_3 photoanode. This is quite helpful in shortening the transit time of minority carrier in the space-charge layer and will effectively reduce the recombination probability of photogenerated electrons and holes during the PEC water oxidation process.[21,48]

The $J-V$ plots of the α-Fe_2O_3 and x-TiO_2@Ti:α-Fe_2O_3 photoanodes as well as their IPCEs at a bias of 1.23 V vs RHE were recorded to evaluate their performance for the PEC water splitting (Figure 3a,b). The dark response for all of the photoanodes is negligible up to about 1.6 V vs RHE. Under simulated AM 1.5G sunlight illumination, both the current densities and the IPCEs of the x-TiO_2@Ti:α-Fe_2O_3 photoanodes are significantly higher than those of the α-Fe_2O_3 photoanode. The 0.5%-TiO_2@Ti:α-Fe_2O_3 photoanode exhibits the highest PEC activity with a photocurrent density of 0.70 ± 0.07 mA cm^{-2} at a bias of 1.23 V vs RHE, which is more than 4 times the magnitude of the α-Fe_2O_3 photoanode (0.16 ± 0.02 mA cm^{-2}) and larger than that of the porous hematite photoanode prepared by the SiO_2 confinement layer strategy.[30] Also, its IPCE value at 370 nm (15.3%) far exceeds that of the α-Fe_2O_3 photoanode (<2%). Thus, the beneficial effect of the Ti-containing layer encapsulation approach in promoting the PEC performance of the hematite photoanode is conspicuous. We emphasize that the results are reproducible. It is consistently observed on more than three electrodes from three batches of samples, and the plots given are the representative results.

The water-splitting current density of a photoelectrode (J_{H_2O}) is a product of the rate of photon absorption expressed as a current density ($J_{absorbed}$), the charge separation efficiency of the photogenerated carriers (η_{sep}), and the charge injection efficiency to the electrolyte (η_{inj}).[7,8] To shed light on the fundamental reason behind the remarkable enhancement in the PEC performance, we measured the UV−vis absorption spectra of the prepared photoanodes. All of the x-TiO_2@Ti:α-Fe_2O_3 photoanodes have slightly lower absorbance than the α-Fe_2O_3 photoanode (Figure S7). Thus, the contribution of light absorption to the improved PEC activity can be excluded. The IPCE increase of the x-TiO_2@Ti:α-Fe_2O_3 photoanodes should be attributed to the promoted charge separation inside the bulk hematite photoanode and/or the enhanced hole transfer across the hematite−electrolyte interface. So, we employed EIS to investigate the behavior of photogenerated charge carriers in these photoanodes.[49−51] It is clear from Figure 3c that for the x-TiO_2@Ti:α-Fe_2O_3 photoanodes the semicircles in the Nyquist plots recorded at 1.23 V vs RHE are all much smaller than those of the α-Fe_2O_3 photoanode, displaying the promoted separation and/or transfer of charge carriers, and the radius of the semicircle first decreases to its minimum value at $x = 0.5\%$ and then increases with increasing x value. The EIS data were also fitted by an equivalent circuit model of the illuminated hematite−electrolyte interface with surface states on the hematite photoanode (Figure 3d) because the hole-transfer step leading to water oxidation was already proven to take place predominantly from surface state holes instead of from valence band holes.[50,52] The equivalent components include the system resistance R_s, the bulk charge-trapping resistance R_{bulk}, the lumped capacitance of the space-charge layer and the Helmholtz layer C_{bulk}, the charge-transfer resistance across the hematite−electrolyte interface R_{ct}, and the capacitance associated with surface states C_{ss}. Both R_{bulk} and R_{ct} of the x-TiO_2@Ti:α-Fe_2O_3 photoanodes are smaller than those of the α-Fe_2O_3 photoanode, explicitly suggesting that both separation and transfer of charge carriers are promoted in the x-TiO_2@Ti:α-Fe_2O_3 photoanode. Moreover, both quickly decrease to their minimum values at $x = 0.5\%$ and then increase with increasing x value (Figure 3e), consistent with the

changing trend of the semicircle radius in the Nyquist plots. Meanwhile, the C_{ss} of the 0.5%-TiO$_2$@Ti:α-Fe$_2$O$_3$ photoanode is obviously higher than that of the α-Fe$_2$O$_3$ photoanode, implying the increase in the amount of surface states active for holes transfer to trigger the water oxidation half-reaction, which is beneficial for transferring holes across the hematite–electrolyte interface. This is in agreement with the increase in the physical surface area of the 0.5%-TiO$_2$@Ti:α-Fe$_2$O$_3$ photoanode compared to that of the α-Fe$_2$O$_3$ photoanode (Table S1).[53] Hence, we conclude that both separation of photogenerated charge carriers inside the bulk hematite photoanode and transfer of holes across the hematite–electrolyte interface have been promoted in the x-TiO$_2$@Ti:α-Fe$_2$O$_3$ photoanodes, thereby leading to significantly larger photocurrent densities than the α-Fe$_2$O$_3$ photoanode. Hereinto, the 0.5%-TiO$_2$@Ti:α-Fe$_2$O$_3$ photoanode displays the best PEC performance because of the most outstanding charge transport property.

We further experimentally quantified the charge separation and injection efficiency of the photoanodes under different applied biases using a widely accepted hole scavenger approach.[7] The enhancement in the charge separation efficiency of the 0.5%-TiO$_2$@Ti:α-Fe$_2$O$_3$ photoanode compared to that of the α-Fe$_2$O$_3$ photoanode is evident in the whole variation range of the external bias (Figure 3f), and the charge separation efficiency (5.53%) of the 0.5%-TiO$_2$@α-Fe$_2$O$_3$ photoanode at 1.23 V vs RHE is more than 2 times the magnitude of the α-Fe$_2$O$_3$ photoanode (2.29%). This is rational as decreasing the crystal feature size of α-Fe$_2$O$_3$ and doping of Ti into its crystal lattice are both greatly beneficial for the suppression of charge recombination within the bulk hematite photoanode. As for the charge injection efficiency, it is almost 0 in the 0.5%-TiO$_2$@Ti:α-Fe$_2$O$_3$ photoanode at the initial stage and lower than that of the α-Fe$_2$O$_3$ photoanode when the external bias is less than 1.05 V vs RHE (Figure 3g). Afterward, it rises more quickly than that of the α-Fe$_2$O$_3$ photoanode and approaches 80% at the external bias of 1.4 V vs RHE, about 1.3 times the magnitude of the α-Fe$_2$O$_3$ photoanode (60%).

The photocurrent onset potential (V_{onset}) is also an important metric for evaluating the PEC water-splitting performance, which determines the minimum external bias needed to split water into H$_2$ and O$_2$.[54] For a photoanode, a lower photocurrent onset potential is always expected to increase its prospect for large-scale application. However, comparing to that of the α-Fe$_2$O$_3$ photoanode, an anodic shift of about 20 mV in the photocurrent onset potential can be found in the 0.5%-TiO$_2$@Ti:α-Fe$_2$O$_3$ photoanode (Figure S8). Generally, the photocurrent onset potential of the hematite photoanode will shift toward more anodic values with increasing bulk charge recombination, increasing charge recombination at the hematite–electrolyte interface, raising flat-band potential, reducing photovoltage, and/or delaying oxygen evolution reaction kinetics.[37,38,55−58] To account for the anodic shift of the photocurrent onset potential, the former four affecting factors will be investigated one by one, without considering oxygen evolution reaction kinetics due to the absence of electrocatalysts in our case. It is clear that the bulk charge recombination in the 0.5%-TiO$_2$@Ti:α-Fe$_2$O$_3$ photoanode is suppressed in comparison to that of the α-Fe$_2$O$_3$ photoanode (Figure 3f). Meanwhile, the transient photocurrent spikes evident in the J−V curves of the α-Fe$_2$O$_3$ photoanode under chopped light illumination, a typical representation of the surface charge recombination,[49] completely disappear in the

0.5%-TiO$_2$@Ti:α-Fe$_2$O$_3$ photoanode, implying the effective suppression of the surface charge recombination by TiO$_2$ encapsulation (Figure S9).[7,49,59,60] That is, the reduced charge recombination both in the bulk hematite photoanode and at the hematite–electrolyte interface cannot cause the anodic shift of the photocurrent onset potential. Then, we explored the changes of the flat-band potentials and the photovoltages in the photoanodes. A positive shift of the flat-band potential (about 10 mV) can be found in the Mott–Schottky plot of the 0.5%-TiO$_2$@Ti:α-Fe$_2$O$_3$ photoanode in comparison to that of the α-Fe$_2$O$_3$ photoanode (Table S1 and Figure S5), and the photovoltage generated in the 0.5%-TiO$_2$@Ti:α-Fe$_2$O$_3$ (130 mV) photoanode is 40 mV smaller than that of the α-Fe$_2$O$_3$ (170 mV) photoanode (Figure S10). Therefore, the raise of the flat-band potential and the decrease in the photovoltage together should lead to an anodic shift of about 50 mV in the photocurrent onset potential of the 0.5%-TiO$_2$@Ti:α-Fe$_2$O$_3$ photoanode compared to that of the α-Fe$_2$O$_3$ photoanode. Taken together, an anodic shift of about 20 mV in the photocurrent onset potential of the 0.5%-TiO$_2$@Ti:α-Fe$_2$O$_3$ photoanode compared to the α-Fe$_2$O$_3$ photoanode is found because the anodic shift of about 50 mV caused by the variations in the flat-band potential and photovoltage is partially compensated by the suppressed charge recombination both within the bulk hematite photoanode and at the hematite–electrolyte interface. Notably, the photovoltage decrease plays a dominant role in the anodic shift.

We speculated that the TiO$_2$ encapsulation layer formed on the surface of the 0.5%-TiO$_2$@Ti:α-Fe$_2$O$_3$ photoanode caused the photovoltage loss.[61,62] This is verified by the surface valence band spectra in Figure S11. The valence band maximum (VBM) of the 0.5%-TiO$_2$@Ti:α-Fe$_2$O$_3$ photoanode (1.52 eV below the Fermi level) is located more positively than that of the α-Fe$_2$O$_3$ photoanode (1.23 eV below the Fermi level), evidencing the existence of hole injection barrier between the bulk hematite and the electrolyte. Because of the charge injection barrier at the Fe$_2$O$_3$−TiO$_2$ interface, a characteristic charge density as well as electric field is required for a given leakage current density. If the potential applied on the photoanode is not positive enough to achieve the required leakage current, potential loss occurs in the TiO$_2$ layer: $\Delta V = \frac{\Delta Q}{\varepsilon_0 \varepsilon_r A} d$, where ΔQ is the increased charge, A is the junction area, ε_0 is the vacuum permittivity, ε_r is the relative permittivity of TiO$_2$, and d is the thickness of the TiO$_2$ layer.[62] Then, the change in the charge injection efficiency can be understood by decomposing the photocurrent at different bias voltages (Figure 3g). At the lower bias voltage ($V < V_{onset}$), the tunneling current is dominant in the total photocurrent. The charge barriers in the 0.5%-TiO$_2$@Ti:α-Fe$_2$O$_3$ photoanode hinder the interface charge transfer and lead to smaller charge injection efficiency than the one in the α-Fe$_2$O$_3$ photoanode. At the higher bias voltage ($V \gg V_{onset}$), the drift-diffusion process prevails over the tunneling process and the interface charge transfer becomes easier for the doped electrode materials compared to α-Fe$_2$O$_3$ because of higher carrier densities, so the charge injection efficiency in the 0.5%-TiO$_2$@Ti:α-Fe$_2$O$_3$ photoanode surpasses the charge injection efficiency in the α-Fe$_2$O$_3$ photoanode.

According to the potential loss formula, a thinner TiO$_2$ layer will result in a smaller potential penalty and a more negative onset potential. Thus, it is necessary to seek a suitable approach to remove the TiO$_2$ encapsulation layer so as to solve the

Scheme 2. Mechanism of Charge Generation, Recombination, and Transport Processes at a Bias of 1.23 V vs RHE in (a) α-Fe$_2$O$_3$, (b) TiO$_2$@Ti:α-Fe$_2$O$_3$, and (c) Ti:α-Fe$_2$O$_3$ Photoanodes[a]
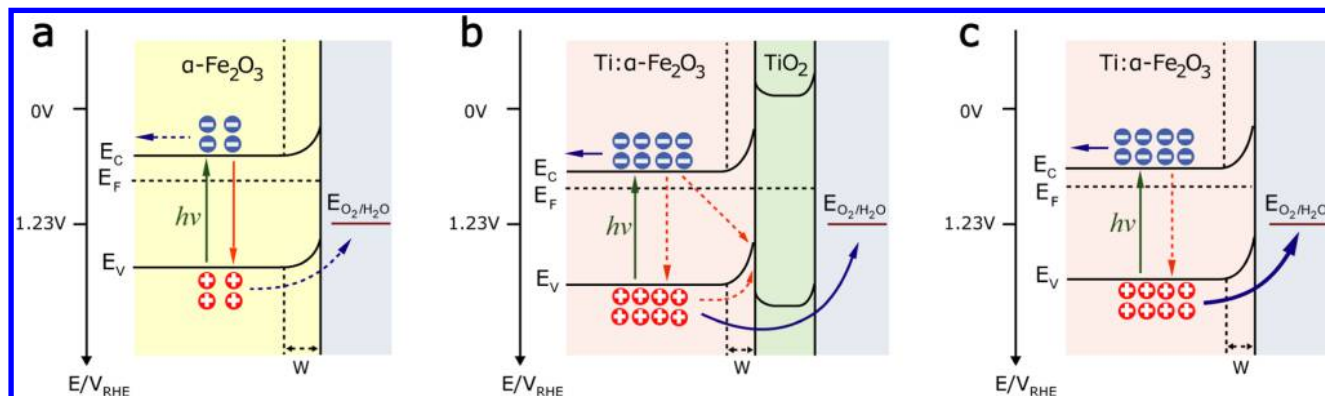
[a]The green, red, and blue arrows refer to the charge generation, recombination, and transport processes, respectively, whereas the dashed and solid lines indicate the relative rates of the charge transport and recombination processes, in which the former represents the slower or impeded rates and the latter represents the faster rates. "W" represents the width of the depletion layer.

problem of the anodic shift of the photocurrent onset potential in the x-TiO$_2$@Ti:α-Fe$_2$O$_3$ photoanodes. On the basis of our previous report,[63] we developed a simple H$_2$O$_2$ solution soaking approach to remove TiO$_2$ on the surface of the 0.5%-TiO$_2$@Ti:α-Fe$_2$O$_3$ photoanode as TiO$_2$ can be dissolved into peroxotitanium acid in H$_2$O$_2$ solution (see the detailed analysis and optimization of H$_2$O$_2$ treatment of the photoanodes in Figures S14 and S15). From the SEM images of the Ti:α-Fe$_2$O$_3$ photoanode (third row in Figure 1a), we see that those platelike nanocrystals with sizes around 100 nm on the surface of the 0.5%-TiO$_2$@Ti:α-Fe$_2$O$_3$ photoanode (second row in Figure 1a) completely disappear after H$_2$O$_2$ soaking treatment for 24 h, accompanied with a notable reduction in the intensity of the Ti 2p XPS peaks (Figure S12), suggesting the dissolution of the TiO$_2$ encapsulation layer. Meanwhile, the H$_2$O$_2$ soaking method has little effect on the bulk physicochemical properties of the 0.5%-TiO$_2$@Ti:α-Fe$_2$O$_3$ photoanode, as evidenced by the similar feature size (Figure S3), XRD pattern (Figure 1b), Mott−Schottky curve (Figures 2c and S5), and UV−vis absorption spectra (Figure S13) compared to those of the 0.5%-TiO$_2$@Ti:α-Fe$_2$O$_3$ photoanode. We see a negative VBM shift of about 210 meV (1.31 eV below the Fermi level) from the surface valence band spectra of the Ti:α-Fe$_2$O$_3$ photoanode (Figure S11) in comparison to that of the 0.5%-TiO$_2$@Ti:α-Fe$_2$O$_3$ photoanode. That is, the hole injection barrier that hinders the transfer of holes from the bulk hematite to the electrolyte has been almost completely removed after H$_2$O$_2$ treatment. As a result, a 30 mV cathodic shift from 0.88 to 0.85 V vs RHE is found in the photocurrent onset potential of the 0.5%-TiO$_2$@Ti:α-Fe$_2$O$_3$ photoanode after H$_2$O$_2$ treatment (Figure S8). We also investigated the change in the photovoltage of the 0.5%-TiO$_2$@Ti:α-Fe$_2$O$_3$ photoanode after H$_2$O$_2$ treatment (Figure S10) and found a photovoltage increase of 30 mV in the Ti:α-Fe$_2$O$_3$ photoanode (160 mV) compared to that of the 0.5%-TiO$_2$@Ti:α-Fe$_2$O$_3$ photoanode (130 mV). This value is equal to the size of the cathodic shift in the photocurrent onset potential after H$_2$O$_2$ treatment, explicitly proving our inference that the anodic shift in the photocurrent onset potential is primarily due to the existence of TiO$_2$ encapsulation layer, which impedes the extraction of holes from the bulk hematite to the electrolyte. Benefitting from the removal of the hole injection barrier, the photocurrent density at 1.23 V vs RHE and the IPCE value at 370 nm of the Ti:α-

Fe$_2$O$_3$ photoanode reach up to 0.83 ± 0.04 mA cm^{-2} and 19%, which are higher than those of the 0.5%-TiO$_2$@Ti:α-Fe$_2$O$_3$ photoanode by 17 and 25%, respectively. Compared to the photocurrent density, IPCE is a more valid figure of merit for PEC device.[8] As shown in Table S2, our IPCE value here is comparable to the best reported ones (related discussion in the Supporting Information). Meanwhile, the representative charge separation efficiency at 1.23 V vs RHE of the Ti:α-Fe$_2$O$_3$ photoanode achieves 7.24% (Figure 3f), which is 1.3 times the magnitude of the 0.5%-TiO$_2$@Ti:α-Fe$_2$O$_3$ photoanode (5.53%). And the charge injection efficiency of the Ti:α-Fe$_2$O$_3$ photoanode is higher than that of the 0.5%-TiO$_2$@Ti:α-Fe$_2$O$_3$ photoanode.

With the above information, the photogenerated charge-carrier generation, recombination, and transport processes in the α-Fe$_2$O$_3$, TiO$_2$@Ti:α-Fe$_2$O$_3$, and Ti:α-Fe$_2$O$_3$ photoanodes are illustrated in Scheme 2. In comparison to the α-Fe$_2$O$_3$ photoanode (Scheme 2a), the introduction of the facile Ti-containing layer encapsulation approach for the preparation of TiO$_2$@Ti:α-Fe$_2$O$_3$ photoanode leads to a significant increase in the electron concentration, which shifts the Fermi level toward the conduction band,[64,65] increases the degree of band bending,[66,67] and improves the conductivity of the photoanodes, greatly facilitating the separation of the photogenerated electron−hole pairs in the space-charge layer (Scheme 2b). Meanwhile, owing to the notable decrease in the crystal feature size, the shortened hole collection distance also improves the proportion of holes that survived to the hematite−electrolyte interface. Hence, the separation efficiency of photogenerated charge carriers in the TiO$_2$@Ti:α-Fe$_2$O$_3$ photoanode is significantly increased in comparison to that of the α-Fe$_2$O$_3$ photoanode. In addition, the transfer of holes across the hematite−electrolyte interface in this photoanode is also enhanced owing to the augmentation of the surface area, which is stemmed from the decreased crystal feature size. Therefore, the TiO$_2$@Ti:α-Fe$_2$O$_3$ photoanode exhibits a remarkably enhanced PEC activity comparing to the α-Fe$_2$O$_3$ photoanode. However, owing to the more positive valence band maximum of TiO$_2$ than α-Fe$_2$O$_3$, a hole injection barrier exists between Ti:α-Fe$_2$O$_3$ and the electrolyte, which hinders the transfer of holes from the bulk hematite to the electrolyte, ultimately causes a loss of the photovoltage in the TiO$_2$@Ti:α-Fe$_2$O$_3$ photoanode, and leads to an anodic shift of the

photocurrent onset potential. Finally, with the successful removal of this hole injection barrier (Scheme 2c), the photogenerated holes transfer from the bulk hematite to the electrolyte solution without hindrance in the Ti:α-Fe$_2$O$_3$ photoanode, further promoting the PEC water-splitting performance by enhancing both the separation and injection efficiencies of photogenerated charge carriers.

4. CONCLUSIONS

We used the α-Fe$_2$O$_3$ photoanode with wormlike nanostructures as a model system and achieved effective suppression of the crystal overgrowth, doping of Ti element into its crystal lattice, as well as repression of the adverse effect on the photocurrent onset potential via a facile sacrificial interlayer approach. These beneficial changes synergistically promote the separation of photogenerated charge carriers in the bulk hematite, and the decreased crystal feature size also leads to an increased surface area, facilitating the transfer of holes at the hematite−electrolyte interface. Finally, the utilization efficiency of photogenerated charge carriers was improved, resulting in 5 times enhancement in the water oxidation photocurrent density of the modified α-Fe$_2$O$_3$ photoanode compared to the bare hematite photoanode. For this system, better PEC water oxidation performance can be expected if an efficient water oxidation electrocatalyst was introduced onto the surface of the Ti:α-Fe$_2$O$_3$ photoanode. Our research indicates that understanding the interfacial engineering mechanisms which may influence the PEC device properties is pivotal for reconciling various strategies in a beneficial way and that this simple and cost-effective method can be generalized into other systems aiming for efficient and scalable solar energy conversion.

ASSOCIATED CONTENT

S Supporting Information

The Supporting Information is available free of charge on the ACS Publications website at DOI: 10.1021/acsami.7b13163.

> SEM images; size distributions; characterizations of XRD and XPS; Mott−Schottky plots; physical surface area measurements; UV−vis spectrum; J−V curves; photocurrent onset potentials and open-circuit potential measurements; valance band spectra (PDF)

AUTHOR INFORMATION

Corresponding Author
*E-mail: gongjr@nanoctr.cn.

ORCID Ⓞ

Jian Ru Gong: 0000-0003-1512-4762

Author Contributions

§K.Z., T.D., G.X., L.G., and B.G. contributed equally.

Notes

The authors declare no competing financial interest.

ACKNOWLEDGMENTS

REFERENCES

(1) Grätzel, M. Photoelectrochemical cells. *Nature* **2001**, *414*, 338−344.

(2) Lewis, N. S. Toward Cost-Effective Solar Energy Use. *Science* **2007**, *315*, 798−801.

(3) Walter, M. G.; Warren, E. L.; McKone, J. R.; Boettcher, S. W.; Mi, Q. X.; Santori, E. A.; Lewis, N. S. Solar Water Splitting Cells. *Chem. Rev.* **2010**, *110*, 6446−6473.

(4) Li, Z. S.; Luo, W. J.; Zhang, M. L.; Feng, J. Y.; Zou, Z. G. Photoelectrochemical cells for solar hydrogen production: current state of promising photoelectrodes, methods to improve their properties, and outlook. *Energy Environ. Sci.* **2013**, *6*, 347−370.

(5) Osterloh, F. E. Inorganic nanostructures for photoelectrochemical and photocatalytic water splitting. *Chem. Soc. Rev.* **2013**, *42*, 2294−2320.

(6) Zhang, K.; Ma, M.; Li, P.; Wang, D. H.; Park, J. H. Water Splitting Progress in Tandem Devices: Moving Photolysis beyond Electrolysis. *Adv. Energy Mater.* **2016**, *6*, No. 1600602.

(7) Dotan, H.; Sivula, K.; Grätzel, M.; Rothschild, A.; Warren, S. C. Probing the photoelectrochemical properties of hematite (α-Fe$_2$O$_3$) electrodes using hydrogen peroxide as a hole scavenger. *Energy Environ. Sci.* **2011**, *4*, 958−964.

(8) Chen, Z.; Deutsch, T. G.; Dinh, H. N.; Domen, K.; Emery, K.; Forman, A. J.; Gaillard, N.; Garland, R.; Heske, C.; Jaramillo, T. F.; Kleiman-Shwarsctein, A.; Miller, E.; Takanabe, K.; Turner, J. *Photoelectrochemical Water Splitting: Standards, Experimental Methods, and Protocols*; Springer New York: New York, NY, 2013; Chapter 2, pp 7−16.

(9) Ager, J. W.; Shaner, M. R.; Walczak, K. A.; Sharp, I. D.; Ardo, S. Experimental demonstrations of spontaneous, solar-driven photoelectrochemical water splitting. *Energy Environ. Sci.* **2015**, *8*, 2811−2824.

(10) Sun, J. W.; Zhong, D. K.; Gamelin, D. R. Composite photoanodes for photoelectrochemical solar water splitting. *Energy Environ. Sci.* **2010**, *3*, 1252−1261.

(11) Zhong, D. K.; Gamelin, D. R. Photoelectrochemical Water Oxidation by Cobalt Catalyst ("Co-Pi")/α-Fe$_2$O$_3$ Composite Photoanodes: Oxygen Evolution and Resolution of a Kinetic Bottleneck. *J. Am. Chem. Soc.* **2010**, *132*, 4202−4207.

(12) Alexander, B. D.; Kulesza, P. J.; Rutkowska, L.; Solarska, R.; Augustynski, J. Metal oxide photoanodes for solar hydrogen production. *J. Mater. Chem.* **2008**, *18*, 2298−2303.

(13) van de Krol, R.; Liang, Y. Q.; Schoonman, J. Solar hydrogen production with nanostructured metal oxides. *J. Mater. Chem.* **2008**, *18*, 2311−2320.

(14) Zhang, J. Z. Metal oxide nanomaterials for solar hydrogen generation from photoelectrochemical water splitting. *MRS Bull.* **2011**, *36*, 48−55.

(15) Sivula, K.; Le Formal, F.; Grätzel, M. Solar Water Splitting: Progress Using Hematite (α-Fe$_2$O$_3$) Photoelectrodes. *ChemSusChem* **2011**, *4*, 432−449.

(16) Lin, Y. J.; Yuan, G. B.; Sheehan, S.; Zhou, S.; Wang, D. W. Hematite-based solar water splitting: challenges and opportunities. *Energy Environ. Sci.* **2011**, *4*, 4862−4869.

(17) Wheeler, D. A.; Wang, G. M.; Ling, Y. C.; Li, Y.; Zhang, J. Z. Nanostructured hematite: synthesis, characterization, charge carrier dynamics, and photoelectrochemical properties. *Energy Environ. Sci.* **2012**, *5*, 6682−6702.

(18) Shen, S. H.; Lindley, S. A.; Chen, X. Y.; Zhang, J. Z. Hematite heterostructures for photoelectrochemical water splitting: rational materials design and charge carrier dynamics. *Energy Environ. Sci.* **2016**, *9*, 2744−2775.

(19) Sivula, K.; Zboril, R.; Le Formal, F.; Robert, R.; Weidenkaff, A.; Tucek, J.; Frydrych, J.; Gratzel, M. Photoelectrochemical Water Splitting with Mesoporous Hematite Prepared by a Solution-Based Colloidal Approach. *J. Am. Chem. Soc.* **2010**, *132*, 7436−7444.

(20) Kim, J. Y.; Magesh, G.; Youn, D. H.; Jang, J. W.; Kubota, J.; Domen, K.; Lee, J. S. Single-crystalline, wormlike hematite photoanodes for efficient solar water splitting. *Sci. Rep.* **2013**, *3*, No. 2681.

(21) Warren, S. C. In *Photoelectrochemical Hydrogen Production*; van de Krol, R., Grätzel, M., Eds.; Springer US: Boston, MA, 2012; Chapter 9, pp 293−316.

(22) Sivula, K. In *Photoelectrochemical Hydrogen Production*; van de Krol, R., Grätzel, M., Eds.; Springer US: Boston, MA, 2012; Chapter 4, pp 121−156.

(23) Franking, R.; Li, L. S.; Lukowski, M. A.; Meng, F.; Tan, Y. Z.; Hamers, R. J.; Jin, S. Facile post-growth doping of nanostructured hematite photoanodes for enhanced photoelectrochemical water oxidation. *Energy Environ. Sci.* 2013, 6, 500−512.

(24) Wang, G.; Ling, Y.; Wheeler, D. A.; George, K. E.; Horsley, K.; Heske, C.; Zhang, J. Z.; Li, Y. Facile synthesis of highly photoactive α-Fe_2O_3-based films for water oxidation. *Nano Lett.* 2011, 11, 3503−3509.

(25) Cho, I. S.; Han, H. S.; Logar, M.; Park, J.; Zheng, X. L. Enhancing Low-Bias Performance of Hematite Photoanodes for Solar Water Splitting by Simultaneous Reduction of Bulk, Interface, and Surface Recombination Pathways. *Adv. Energy Mater.* 2016, 6, No. 1501840.

(26) Wang, L.; Lee, C. Y.; Schmuki, P. Solar water splitting: preserving the beneficial small feature size in porous α-Fe_2O_3 photoelectrodes during annealing. *J. Mater. Chem. A* 2013, 1, 212−215.

(27) Hong, S. J.; Jun, H.; Borse, P. H.; Lee, J. S. Size effects of WO_3 nanocrystals for photooxidation of water in particulate suspension and photoelectrochemical film systems. *Int. J. Hydrogen Energy* 2009, 34, 3234−3242.

(28) Luo, H. M.; Mueller, A. H.; McCleskey, T. M.; Burrell, A. K.; Bauer, E.; Jia, Q. X. Structural and photoelectrochemical properties of $BiVO_4$ thin films. *J. Phys. Chem. C* 2008, 112, 6099−6102.

(29) Hou, Y.; Zheng, C.; Zhu, Z. Z.; Wang, X. C. Microwave-assisted fabrication of porous hematite photoanodes for efficient solar water splitting. *Chem. Commun.* 2016, 52, 6888−6891.

(30) Brillet, J.; Grätzel, M.; Sivula, K. Decoupling Feature Size and Functionality in Solution-Processed, Porous Hematite Electrodes for Solar Water Splitting. *Nano Lett.* 2010, 10, 4155−4160.

(31) Ahn, H. J.; Yoon, K. Y.; Kwak, M. J.; Jang, J. H. A Titanium-Doped SiO_x Passivation Layer for Greatly Enhanced Performance of a Hematite-Based Photoelectrochemical System. *Angew. Chem., Int. Ed.* 2016, 55, 9922−9926.

(32) Cesar, I.; Kay, A.; Martinez, J. A. G.; Gratzel, M. Translucent thin film Fe_2O_3 photoanodes for efficient water splitting by sunlight: Nanostructure-directing effect of Si-doping. *J. Am. Chem. Soc.* 2006, 128, 4582−4583.

(33) Xi, L. F.; Chiam, S. Y.; Mak, W. F.; Tran, P. D.; Barber, J.; Loo, S. C. J.; Wong, L. H. A novel strategy for surface treatment on hematite photoanode for efficient water oxidation. *Chem. Sci.* 2013, 4, 164−169.

(34) Mulmudi, H. K.; Mathews, N.; Dou, X. C.; Xi, L. F.; Pramana, S. S.; Lam, Y. M.; Mhaisalkar, S. G. Controlled growth of hematite (alpha-Fe_2O_3) nanorod array on fluorine doped tin oxide: Synthesis and photoelectrochemical properties. *Electrochem. Commun.* 2011, 13, 951−954.

(35) Bandara, J.; Mielczarski, J. A.; Kiwi, J. 1. Molecular mechanism of surface recognition. Azo dyes degradation on Fe, Ti, and Al oxides through metal sulfonate complexes. *Langmuir* 1999, 15, 7670−7679.

(36) Kay, A.; Cesar, I.; Grätzel, M. New benchmark for water photooxidation by nanostructured α-Fe_2O_3 films. *J. Am. Chem. Soc.* 2006, 128, 15714−15721.

(37) Jang, J. W.; Du, C.; Ye, Y. F.; Lin, Y. J.; Yao, X. H.; Thorne, J.; Liu, E.; McMahon, G.; Zhu, J. F.; Javey, A.; Guo, J. H.; Wang, D. W. Enabling unassisted solar water splitting by iron oxide and silicon. *Nat. Commun.* 2015, 6, No. 7447.

(38) Du, C.; Yang, X. G.; Mayer, M. T.; Hoyt, H.; Xie, J.; McMahon, G.; Bischoping, G.; Wang, D. W. Hematite-Based Water Splitting with Low Turn-On Voltages. *Angew. Chem., Int. Ed.* 2013, 52, 12692−12695.

(39) Wang, K. X. Z.; Wu, Z. F.; Liu, V.; Brongersma, M. L.; Jaramillo, T. F.; Fan, S. H. Nearly Total Solar Absorption in Ultrathin Nanostructured Iron Oxide for Efficient Photoelectrochemical Water Splitting. *ACS Photonics* 2014, 1, 235−240.

(40) Iordanova, N.; Dupuis, M.; Rosso, K. M. Charge transport in metal oxides: A theoretical study of hematite α-Fe_2O_3. *J. Chem. Phys.* 2005, 122, No. 144305.

(41) Kronawitter, C. X.; Zegkinoglou, I.; Shen, S. H.; Liao, P.; Cho, I. S.; Zandi, O.; Liu, Y. S.; Lashgari, K.; Westin, G.; Guo, J. H.; Himpsel, F. J.; Carter, E. A.; Zheng, X. L.; Hamann, T. W.; Koel, B. E.; Mao, S. S.; Vayssieres, L. Titanium incorporation into hematite photoelectrodes: theoretical considerations and experimental observations. *Energy Environ. Sci.* 2014, 7, 3100−3121.

(42) Giannuzzi, L. A.; Stevie, F. A. A review of focused ion beam milling techniques for TEM specimen preparation. *Micron* 1999, 30, 197−204.

(43) Sanjinés, R.; Tang, H.; Berger, H.; Gozzo, F.; Margaritondo, G.; Levy, F. Electronic-Structure of Anatase TiO_2 Oxide. *J. Appl. Phys.* 1994, 75, 2945−2951.

(44) Pownceby, M. I.; Constanti-Carey, K. K.; Fisher-White, M. J. Subsolidus phase relationships in the system Fe_2O_3-Al_2O_3-TiO_2 between 1000° and 1300°C. *J. Am. Ceram. Soc.* 2003, 86, 975−980.

(45) Liao, P.; Toroker, M. C.; Carter, E. A. Electron Transport in Pure and Doped Hematite. *Nano Lett.* 2011, 11, 1775−1781.

(46) Gomes, W. P.; Cardon, F. Electron-Energy Levels in Semiconductor Electrochemistry. *Prog. Surf. Sci.* 1982, 12, 155−215.

(47) Cesar, I.; Sivula, K.; Kay, A.; Zboril, R.; Grätzel, M. Influence of Feature Size, Film Thickness, and Silicon Doping on the Performance of Nanostructured Hematite Photoanodes for Solar Water Splitting. *J. Phys. Chem. C* 2009, 113, 772−782.

(48) Jarrett, H. S. Photocurrent Conversion Efficiency in a Schottky-Barrier. *J. Appl. Phys.* 1981, 52, 4681−4689.

(49) Klahr, B.; Gimenez, S.; Fabregat-Santiago, F.; Bisquert, J.; Hamann, T. W. Electrochemical and photoelectrochemical investigation of water oxidation with hematite electrodes. *Energy Environ. Sci.* 2012, 5, 7626−7636.

(50) Klahr, B.; Gimenez, S.; Fabregat-Santiago, F.; Hamann, T.; Bisquert, J. Water Oxidation at Hematite Photoelectrodes: The Role of Surface States. *J. Am. Chem. Soc.* 2012, 134, 4294−4302.

(51) Iandolo, B.; Hellman, A. The Role of Surface States in the Oxygen Evolution Reaction on Hematite. *Angew. Chem., Int. Ed.* 2014, 53, 13404−13408.

(52) Steier, L.; Herraiz-Cardona, I.; Gimenez, S.; Fabregat-Santiago, F.; Bisquert, J.; Tilley, S. D.; Grätzel, M. Understanding the Role of Underlayers and Overlayers in Thin Film Hematite Photoanodes. *Adv. Funct. Mater.* 2014, 24, 7681−7688.

(53) Pinaud, B. A.; Vesborg, P. C. K.; Jaramillo, T. F. Effect of Film Morphology and Thickness on Charge Transport in Ta_3N_5/Ta Photoanodes for Solar Water Splitting. *J. Phys. Chem. C* 2012, 116, 15918−15924.

(54) Tilley, S. D.; Cornuz, M.; Sivula, K.; Gratzel, M. Light-Induced Water Splitting with Hematite: Improved Nanostructure and Iridium Oxide Catalysis. *Angew. Chem., Int. Ed.* 2010, 49, 6405−6408.

(55) Thorne, J. E.; Li, S.; Du, C.; Qin, G. W.; Wang, D. W. Energetics at the Surface of Photoelectrodes and Its Influence on the Photoelectrochemical Properties. *J. Phys. Chem. Lett.* 2015, 6, 4083−4088.

(56) Iandolo, B.; Wickman, B.; Zorić, I.; Hellman, A. The rise of hematite: origin and strategies to reduce the high onset potential for the oxygen evolution reaction. *J. Mater. Chem. A* 2015, 3, 16896−16912.

(57) Le Formal, F.; Tetreault, N.; Cornuz, M.; Moehl, T.; Grätzel, M.; Sivula, K. Passivating surface states on water splitting hematite photoanodes with alumina overlayers. *Chem. Sci.* 2011, 2, 737−743.

(58) Barroso, M.; Mesa, C. A.; Pendlebury, S. R.; Cowan, A. J.; Hisatomi, T.; Sivula, K.; Grätzel, M.; Klug, D. R.; Durrant, J. R. Dynamics of photogenerated holes in surface modified α-Fe_2O_3 photoanodes for solar water splitting. *Proc. Natl. Acad. Sci. U.S.A.* 2012, 109, 15640−15645.

(59) Yang, X.; Liu, R.; Du, C.; Dai, P. C.; Zheng, Z.; Wang, D. W. Improving Hematite-based Photoelectrochemical Water Splitting with

Ultrathin TiO_2 by Atomic Layer Deposition. *ACS Appl. Mater. Interfaces* **2014**, *6*, 12005−12011.

(60) Ahmed, M. G.; Kretschmer, I. E.; Kandiel, T. A.; Ahmed, A. Y.; Rashwan, F. A.; Bahnemann, D. W. A Facile Surface Passivation of Hematite Photoanodes with TiO_2 Overlayers for Efficient Solar Water Splitting. *ACS Appl. Mater. Interfaces* **2015**, *7*, 24053−24062.

(61) Monllor-Satoca, D.; Bartsch, M.; Fabrega, C.; Genc, A.; Reinhard, S.; Andreu, T.; Arbiol, J.; Niederberger, M.; Morante, J. R. What do you do, titanium? Insight into the role of titanium oxide as a water oxidation promoter in hematite-based photoanodes. *Energy Environ. Sci.* **2015**, *8*, 3242−3254.

(62) Scheuermann, A. G.; Lawrence, J. P.; Kemp, K. W.; Ito, T.; Walsh, A.; Chidsey, C. E. D.; Hurley, P. K.; McIntyre, P. C. Design principles for maximizing photovoltage in metal-oxide-protected water-splitting photoanodes. *Nat. Mater.* **2016**, *15*, 99−105.

(63) Zhang, K.; Liu, Q.; Wang, H.; Zhang, R. B.; Wu, C. H.; Gong, J. R. TiO_2 Single Crystal with Four-Truncated-Bipyramid Morphology as an Efficient Photocatalyst for Hydrogen Production. *Small* **2013**, *9*, 2452−2459.

(64) Abdi, F. F.; Han, L. H.; Smets, A. H. M.; Zeman, M.; Dam, B.; van de Krol, R. Efficient solar water splitting by enhanced charge separation in a bismuth vanadate-silicon tandem photoelectrode. *Nat. Commun.* **2013**, *4*, No. 2195.

(65) Meng, X. Y.; Qin, G. W.; Li, S.; Wen, X. H.; Ren, Y. P.; Pei, W. L.; Zuo, L. Enhanced photoelectrochemical activity for Cu and Ti doped hematite: The first principles calculations. *Appl. Phys. Lett.* **2011**, *98*, No. 112104.

(66) Wang, G.; Wang, H. Y.; Ling, Y. C.; Tang, Y. C.; Yang, X. Y.; Fitzmorris, R. C.; Wang, C. C.; Zhang, J. Z.; Li, Y. Hydrogen-Treated TiO_2 Nanowire Arrays for Photoelectrochemical Water Splitting. *Nano Lett.* **2011**, *11*, 3026−3033.

(67) Uchiyama, H.; Yukizawa, M.; Kozuka, H. Photoelectrochemical Properties of Fe_2O_3-SnO_2 Films Prepared by Sol-Gel Method. *J. Phys. Chem. C* **2011**, *115*, 7050−7055.